nature communications

Article

https://doi.org/10.1038/s41467-026-79445-1

Directional motility of crystallizing cholesterol on supported lipid bilayers

Received: 13 April 2026

Accepted: 19 October 2026

Published online: 13 November 2026

Check for updates

Hyunhyuk Tae[1], Younghwan Choe[1], Dongping Jiang[1], Lepakshi Gnanasekaran[1], Soohyun Park[1], Ji-Yu Zhu[2], Guillermo C. Bazan[2,3], Vladimir P. Zhdanov[4], Atul N. Parikh[3,5,6] & Nam-Joon Cho[1]

Cholesterol crystallization within phospholipid bilayers necessarily remodels the surrounding membrane, creating dynamic feedback between growing crystallites and locally changing membrane. Using fluorescence microscopy, we show that lipid-coated, cholesterol-rich crystallites self-propel on the bilayer surface along directional trajectories, including circular, unidirectional, and reciprocating motion. We hypothesize that crystallite motilities arise from local cholesterol depletion in the underlying bilayer, generating gradients in composition, rigidity, and thus adhesion, which induce directional forces analogous to those involved in haptotaxis and/or durotaxis. Fluorescence lifetime imaging with a mechanosensitive probe reveals time-resolved changes in membrane packing, consistent with this mechanism. Single particle tracking and mathematical modeling support the mechanical plausibility of a working model in which crystallization-induced cholesterol redistribution may generate dynamic rigidity gradients at crystallite–membrane interface. Tuning membrane states yields a quantitative operating map that relates composition to motility, providing model-dependent design guidance for controlling cholesterol crystallite transport on lipid interfaces.

Phase transformation in living systems often occurs under spatial or dimensional confinement of a structure-directing template. Compared with bulk homogeneous solution, crystallization confined to compartmentalized volumes or low-dimensional interfaces – including surfaces, pores, droplets, condensates, micelles, vesicles, and membranes – experiences constraints: finite size, transport limitations, and proximal boundaries. Together, these constraints alter nucleation, modulate growth kinetics, and produce distinct morphologies and polymorphs with, often, no comparable counterpart in the bulk. This is perhaps best appreciated in the many contexts of biomineralization[1–3], where the spatial and dimensional constraints of a template direct the formation of biominerals of diverse habits, unusual microstructures, and varied functionalities.

From a system perspective, it is clear that crystallization necessarily alters the template that directs the process. This scenario is particularly acute in crystallization confined to limited volumes and fixed surfaces, creating a dynamic – ever shifting – interplay between growing crystals and the changing properties of the template. But how this interplay influences phase transformation is, in general, not well understood. Here, we consider crystallization of cholesterol within supported lipid bilayers (SLBs) mimicking cellular membranes[4,5]—a molecularly

[1]School of Materials Science and Engineering, Nanyang Technological University, Singapore, Singapore. [2]Department of Chemistry, National University of Singapore, Singapore, Singapore. [3]Institute for Digital Molecular Analytics and Science, Nanyang Technological University, Singapore, Singapore. [4]Boreskov Institute of Catalysis, Russian Academy of Sciences, Novosibirsk, Russia. [5]Department of Biomedical Engineering, University of California, Davis, California, USA. [6]Singapore Centre for Environmental Life Sciences Engineering, Nanyang Technological University, Singapore, Singapore.
e-mail: njcho@ntu.edu.sg

crowded, quasi-two-dimensional interfacial environment. Beyond its importance, this system is biomedically significant in diverse pathophysiology, including atherosclerosis[6,7], gallstone formation[8], and age-related macular degeneration[9], and accordingly is of interest to biochemical engineering.

When cholesterol levels in cellular membranes exceed their solubility limit, supersaturation drives the nucleation of cholesterol clusters within the bilayer[6,9–11]. These prenucleation clusters grow to form two-dimensional (2D) crystallites and, ultimately, three-dimensional (3D) cholesterol crystals[5,7,12–16]. The kinetic pathways of these transformations depend on a number of factors, including cholesterol supersaturation, lipid composition, and the biophysical properties of the lipid bilayer including lateral diffusivity, phase state (e.g., gel, fluid, or liquid-crystalline), and the presence, sizes, and distributions of phase-separated domains[16,17]. In recent studies, we and others found that cholesterol crystallization on membranes follows a complicated kinetic pathway[18–20]. En route to the formation of the thermodynamically stable quadrilateral plate structures, the pathway funnels through a multistep staircase cascade – with each successive phase transition incurring the smallest loss of free energy relative to its predecessor – as predicted by the Ostwald's rule of stages[18].

As discussed above, crystallization of cholesterol alters the template – the lipid bilayer – itself. As cholesterol crystallization proceeds, the bilayer becomes locally (and ultimately globally) depleted in cholesterol. This real-time change in membrane composition induces corresponding local changes in the membrane biophysical properties, such as fluidity and tension, which equilibrate across the membrane[4,21–23]. These alterations are integral to the crystallization process. However, the feedback mechanisms by which these membrane property changes influence crystal growth and behavior have yet to be elucidated.

In this work, we find that lipid-coated cholesterol-rich crystallites exhibit directional motility on the membrane surface. Cholesterol-rich crystallizing structures emerging from the membrane interface self-propel along recognizable trajectories, including circular, unidirectional, and reciprocating motion. While various directed motions in a crowded environment[24] and specific cases such as lamellipodial extension and vesicular transport[25–27] have long been understood in cellular systems, comparable dynamic behaviors in the context of phase change, such as cholesterol crystallization, have not, to our knowledge, been reported. We propose that these movements arise from dynamically generated gradients in membrane rigidity and stiffness. Specifically, as crystallites grow, cholesterol depletes locally in the proximity of the crystal-membrane interface – a notion supported by our fluorescence lifetime imaging microscopy (FLIM) measurements using a mechanosensitive probe. This, in turn, may create shifting gradients in composition and mechanical properties that contribute to crystallite motility – reminiscent of durotaxis or haptotaxis, in which cellular migration is guided by gradients in substrate stiffness or adhesion, respectively[28,29]. Single particle tracking combined with mathematical modeling further supports the mechanical plausibility of this gradient-based working model. These insights then translate into empirical design guidance for cholesterol crystallite motility. By tuning membrane state from fluid to rigid, we construct a quantitative operating map that links lipid composition to motility outputs. Methyl-β-cyclodextrin–mediated cholesterol transfer further provides on-demand motility control by reactivating arrested crystallites. Together, these results establish a programmable strategy for autonomous transport on soft interfaces, connecting interfacial phase transformation to actionable principles in chemical engineering and offering a route to phase transformation-driven material transport.

Results

Dynamic Directional Motility of Cholesterol Crystallites

We began by preparing 1,2-dioleoyl-sn-glycero-3-phosphocholine (DOPC) membranes with supersaturated cholesterol, far exceeding solubility limits within the phosphatidylcholine (PC) bilayer (~ 66 mol %)[10], thereby enabling subsequent nucleation and growth of surface-bound cholesterol-rich crystallizing structures (Fig. 1A). For comparison, our previous study showed that supported lipid bilayers formed from bicellar mixtures containing 10–60 mol% cholesterol, below the reported cholesterol solubility limit in phosphatidylcholine bilayers, without detectable cholesterol crystallization (see Fig. 3 in Ref. 30). This comparison supports the use of 80 mol% cholesterol to access the supersaturated, crystallization-capable regime examined here. This was achieved using a well-established methodology to form supported lipid bilayers (SLBs) through the adsorption, rupture, and fusion of self-assembled bicellar precursors[18,30–32]. Briefly, the cholesterol-enriched bicellar mixtures were flowed onto a silica surface. Their spontaneous adsorption, fusion, and coalescence formed SLB patches, which became laterally contiguous, ultimately producing SLBs supersaturated in cholesterol (Suppl. Fig. 1). Previous studies have established that during crystallization, the structural integrity of the SLBs is preserved[18]. Because these cholesterol-loaded SLBs are thermodynamically unstable, they spontaneously evolve crystallizing cholesterol from the membrane phase. The process was readily visualized by incorporating 0.5 mol% 1,2-dipalmitoyl-sn-glycero-3-phosphoethanolamine-N-(lissamine rhodamine B sulfonyl) (ammonium salt) (Rh-PE) into the precursor bicellar mixtures (Suppl. Movie 1). The resulting cholesterol-rich crystallizing structures precipitated from the SLB environment, producing surface-bound crystallites[33], in full agreement with previous observations.

During crystallization, three distinct features were observed: a continuous fluorescent membrane background, dark spindle- or plate-like structures, and fluorescent rod-shaped objects. The dark structures exhibited morphologies consistent with crystalline cholesterol reported previously[7,34], whereas the bright rod-like features appeared as elongated fluorescent entities positioned above the membrane surface. Prior work from our group has established that cholesterol crystallization from supersaturated lipid bilayers proceeds through transient, lipid-covered metastable intermediates, including filamentous and rod-like phases that subsequently evolve into quadrilateral plates of the triclinic polymorph[18]. Consistent with this established crystallization pathway, we interpret both the bright and dark structures observed here as cholesterol crystallites.

Importantly, Rh-PE does not label the interior of the crystalline cholesterol phase. Rather, it reports dye-accessible lipid environments at the SLB and at the membrane–crystallite interface. To verify the identity of both bright and dark objects observed in the Rh-PE channel, we performed cholesterol-specific labeling using BODIPY-cholesterol and observed co-localization with both populations (Suppl. Fig. 2). It allows us to interpret the fluorescently bright rod-like objects as cholesterol crystallites that remain partially lipid-coated during early growth, such that Rh-PE resides in the interfacial lipid layer rather than in the cholesterol lattice. This interpretation is further supported by time-lapse observations in which bright rods lose fluorescence upon contact and merging with dark crystallites, consistent with a decrease in dye-accessible interfacial lipid area (Suppl. Fig. 3). Alternatively, larger crystallites may locally displace the SLB and contact the underlying support, which would eliminate a dye-accessible crystallite–SLB interface and likewise render these crystallites dark. Taken together, these observations support the assignment of the bright rods as lipid-coated, cholesterol-rich nascent crystallites and the dark features as more mature cholesterol-rich structures consistent with cholesterol crystallites. Because neither fluorescence

https://doi.org/10.1038/s41467-026-79445-1

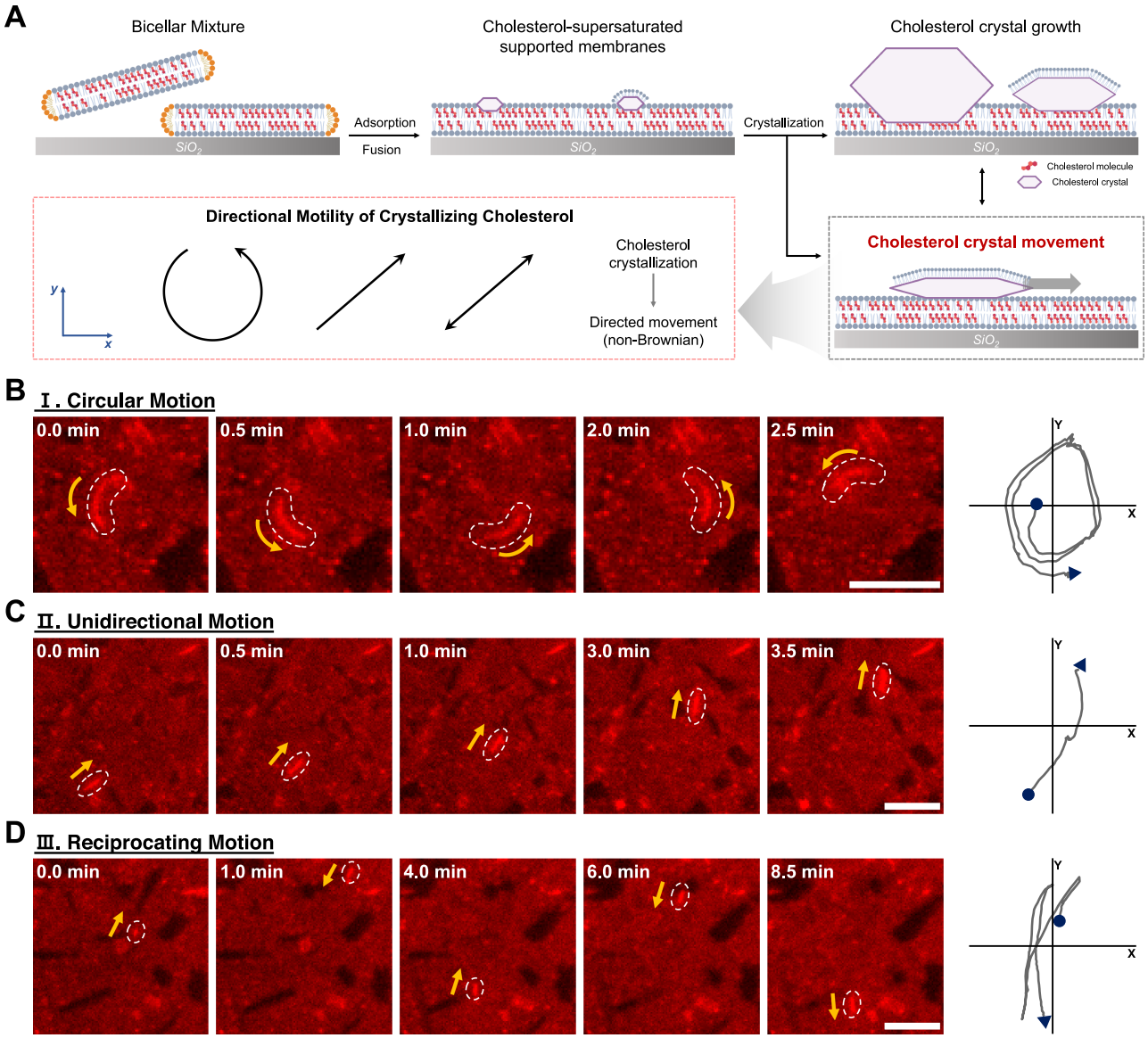

Fig. 1 | Dynamic directional motility of crystallizing cholesterol on DOPC supported lipid membranes. A Schematic illustrating supported membrane formation from supersaturated cholesterol-laden bicellar mixtures, subsequent nucleation and growth of cholesterol-rich crystallizing structures, and emergence of lipid-coated cholesterol-rich nascent crystallites displaying directional motions along the membrane. Created in BioRender. in Translational Science, E. (2026) https://BioRender.com/fsqu7jf (**B**–**D**) Microscopic observations of single crystallites exhibiting (**B**) circular, (**C**) unidirectional and (**D**) reciprocating motions with the full two-dimensional trajectories. In each series, the first image was set to 0 min to follow the motility timeline. Dashed contours delineate the moving crystallite and yellow arrows indicate instantaneous direction. Each panel is representative of three independent supported lipid bilayer preparations that gave similar results. Scale bar, 10 µm.

channel directly resolves the cholesterol lattice, this assignment remains inferential. For concision, we refer to these cholesterol-rich crystallizing structures as crystallites.

During cholesterol crystallization, a subset of fluorescently bright (lipid-coated), rod-shaped cholesterol crystallites became motile on the membrane surface. Furthermore, their trajectories were non-random (non-Brownian), exhibiting recognizable patterns of directed motion. Specifically, some crystallites displayed circular motion, rotating either clockwise or counterclockwise (Fig. 1B and Supplementary Movie 2), while others traveled in a single direction (unidirectional motion; Fig. 1C and Supplementary Movie 3). Some others showed reciprocating motion, reversing directions stochastically and periodically (Fig. 1D and Supplementary Movie 4). These motion types were reproducibly observed across independent experiments (Supplementary Fig. 4).

To quantify these behaviors, we scrutinized 46 single-crystallite tracks ($n = 46$) observed in three independent bilayer preparations (Supplementary Figs. 5–7) and identified three motion types including circular ($n = 13$), unidirectional ($n = 19$), and reciprocating ($n = 14$). The onset and duration of crystallite movements displayed notable variability, with a mean duration of 5.3 ± 4.5 min without a single characteristic timescale (Fig. 2A). When categorized by motion type, the durations were 5.9 ± 4.5 min for circular motion, 2.7 ± 1.8 min for unidirectional motion, and 8.1 ± 5.2 min for reciprocating motion (Fig. 2B). Unidirectional motions were shorter than circular and reciprocating ones, whereas the latter two were comparable. Thus, although duration differs by motion type, duration alone does not determine the specific directional patterns. Instead, they are likely governed by other dynamic factors, such as the forces acting on the

https://doi.org/10.1038/s41467-026-79445-1

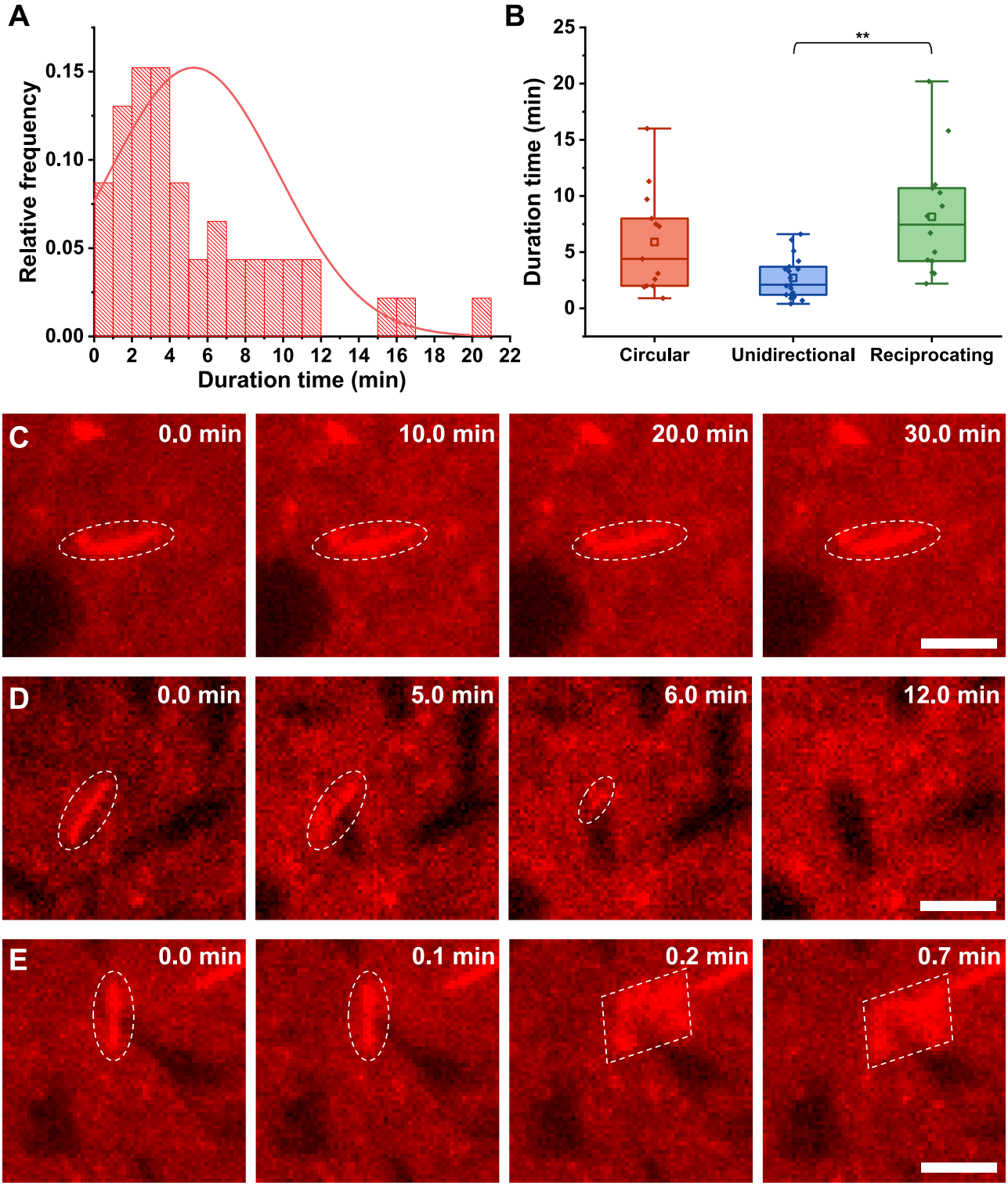

Fig. 2 | Duration of directed motility and post-movement fates of lipid-coated cholesterol-rich crystallites on DOPC supported lipid membranes. **A** Histogram of motility duration for moving crystallites. $n = 46$ individual motile crystallites pooled from three independent supported lipid bilayer preparations; the unit of study is a single tracked crystallite. **B** Motility duration by motion type. $n = 13$ (circular), $n = 19$ (unidirectional) and $n = 14$ (reciprocating) individual motile crystallites, pooled from the same three independent bilayer preparations. In the box plots the centre line denotes the median, the bounds of the box denote the 25th and 75th percentiles, and the whiskers denote the minimum and maximum values lying within 1.5 times the interquartile range; all individual crystallite values are overlaid as points. Groups were compared using Welch's one-way ANOVA followed by two-sided Games–Howell multiple-comparisons tests. Multiplicity-adjusted P-values: circular versus unidirectional, $P = 0.0718$; circular versus reciprocating, $P = 0.466$; unidirectional versus reciprocating, $P = 0.0050$. Asterisks denote $^{*}P < 0.05$, $^{**}P < 0.01$ and $^{***}P < 0.001$. **C**–**E** Microscopic observations of dynamic post-movement behaviours, depicting (**C**) stop-and-stay at the membrane surface, (**D**) dissolution into cholesterol-enriched membrane domains and (**E**) morphological transformation into quadrilateral plates; each panel is representative of three independent bilayer preparations that gave similar results. In each series, t = 0 min denotes the first frame after directed motion ceased. Scale bar, 5 µm. Source data are provided as a Source Data file.

https://doi.org/10.1038/s41467-026-79445-1

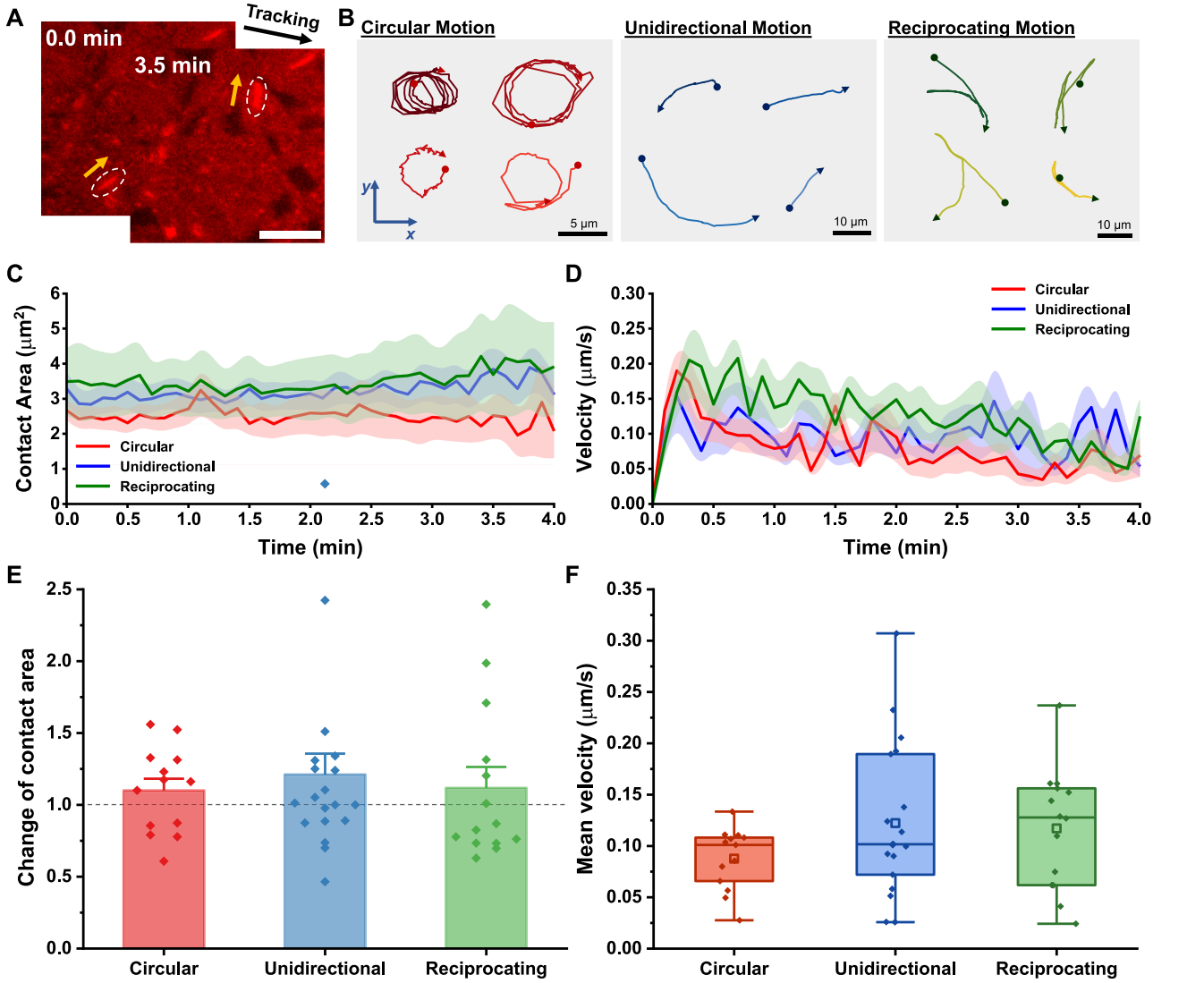

Fig. 3 | Single particle tracking analysis of cholesterol crystallite motility on DOPC supported lipid membranes. A Schematic representation of microscopic imaging capturing cholesterol crystallite motility and corresponding fluorescence traces for the indicated crystallite; the traces are representative of three independent bilayer preparations that gave similar results. Scale bar, 10 μm. **B** Exemplary trajectories illustrating circular, unidirectional and reciprocating motions (filled dot, start; arrowheads, direction). Trajectories for all tracked crystallites are shown in Supplementary Fig. 8. **C** Contact area with lipid membranes and **D** instantaneous velocity versus time for each motion type; thick lines denote the mean and shaded bands denote the mean ± SEM, with data shown to 4 min. **E** Fold-change in contact area after motion relative to the initial value, presented as mean values ± s.e.m. with all individual crystallite values overlaid as points. **F** Box plots of mean velocity by motion type, in which the centre line denotes the median, the bounds of the box denote the 25th and 75th percentiles and the whiskers denote the minimum and maximum values lying within 1.5 times the interquartile range, with all individual crystallite values overlaid as points. In (**C**–**F**), $n = 13$ (circular), $n = 19$ (unidirectional) and $n = 14$ (reciprocating) individual motile crystallites pooled from three independent supported lipid bilayer preparations; the unit of study is a single tracked crystallite. Source data are provided as a Source Data file.

crystallites, their velocities, and changes in their size during the process.

After losing their motility, crystallites exhibited distinct post-movement behaviors. Some crystallites ceased motion and became stationary for over 30 minutes (Fig. 2C and Supplementary Movie 5), while others appeared to dissolve, possibly by merging with other growing lipid-depleted cholesterol crystallites (Fig. 2D and Supplementary Movie 6). The latter behavior was consistent with the dissolution of cholesterol from the rod phase into the membrane, leading to the formation of cholesterol-enriched domains[35]. Additionally, some rod-shaped crystallites underwent a rapid morphological change, transforming into quadrilateral plates (~0.2 min) immediately after arrest (Fig. 2E and Supplementary Movie 7). Importantly, these post-movement behaviors showed no correlation with the prior motion patterns of the crystallites, indicating that the observed motility and subsequent transitions arise from the interplay between multiple physical and chemical parameters, rather than being directly linked to the spatiotemporal aspect of their movements.

Single particle tracking of cholesterol crystallite motility

Next, we investigated the kinematics of individual crystallites in more detail by single particle tracking (Fig. 3A). The apparent crystallite size in the fluorescence images was interpreted as its contact area with SLBs and was manually quantified frame-by-frame using ImageJ. The velocities of motile crystallites were tracked using the TrackMate plugin in ImageJ[36], with motion patterns categorized according to their trajectory types (Fig. 3B and Supplementary Fig. 8). Time traces of contact area and velocity for all crystallites are provided in Supplementary Fig. 9.

While the initial contact area of crystallites varied at motion onset, afterwards it increased modestly during motion for all types (Fig. 3C). On average, circular trajectories remained nearly constant with slight increases, whereas unidirectional and reciprocating trajectories showed larger increases. Consistently, the fold-change in contact area after motion was >1 for all types, with unidirectional showing the largest positive shift and circular the smallest (Fig. 3E). Quantitatively, mean fold-changes were ≈1.21 for unidirectional, ≈1.12 for reciprocating, and ≈1.10 for circular motion, indicating continued exchange and uptake of cholesterol from the underlying membrane during transport regardless of motion patterns.

Instantaneous velocity of crystallites showed a rapid early transient followed by fluctuating plateaus (Fig. 3D). The velocity distribution revealed type-dependent trends (Fig. 3F). Crystallites with unidirectional motion exhibited the highest mean velocity of 0.122 μm/s, with a relatively broad distribution. In contrast, crystallites with reciprocating and circular motions displayed lower mean velocities of 0.117 μm/s and 0.0877 μm/s, respectively. Despite this ordering in velocity, total displacement was longest for reciprocating trajectories, consistent with their longer duration (see Fig. 2B), whereas unidirectional trajectories, though fastest, covered shorter total displacement on average (Supplementary Fig. 10A). The confinement ratio (net/total displacement) further demonstrates higher path efficiency for unidirectional motion and highlights type-dependent differences (Supplementary Fig. 10B).

To evaluate whether the representative crystallite morphologies were systematically associated with motion type, we quantified the apparent footprint of all tracked crystallites using aspect ratio and solidity (Supplementary Fig. 11). Unidirectional trajectories tended to extend toward larger aspect ratios, whereas circular trajectories tended to include lower-solidity, more irregular footprints. However, neither aspect ratio nor solidity differed significantly among circular, unidirectional, and reciprocating trajectories, and the distributions showed substantial overlap. Aspect ratio exhibited only a weak positive association with the linearity of forward progression. These results indicate that crystallite morphology may weakly bias how motion is expressed but does not uniquely determine trajectory class.

Collectively, these results show that (i) contact area growth accompanies motility; (ii) velocity depends on motion type, with unidirectional trajectories moving most efficiently; and (iii) the net transport scale reflects coupling between path geometry and duration, with reciprocating trajectories achieving the longest displacements via longer duration, and unidirectional trajectories achieving the highest velocity but shorter total displacements.

Membrane rigidity changes during crystallite movements

On lipid bilayers, nanoparticles can display conventional diffusion and/or directed motility through various driving forces, such as liquid flow[37] or charge exchange mechanisms[38]. However, no such driving forces are evident in the movement of micro-sized cholesterol crystallites observed here. Given the supersaturated cholesterol conditions in this system, we hypothesized that cholesterol concentration gradients—either within the membrane or across its regions—serve as the primary drivers of this phenomenon. Specifically, we propose that the surfing-like motility of cholesterol crystallites is mediated by membrane alterations induced by the crystallites themselves. During crystallization, the exchange of cholesterol molecules between crystallites and the surrounding membrane, their redistribution among nearby regions, and their depletion from the membrane dynamically alter local lipid composition and packing, thereby modifying the biophysical properties of the membrane[21,39]. As cholesterol is a well-established regulator of membrane packing[40,41], localized cholesterol removal or shifts in concentration disrupt this packing, consequently generating gradients in membrane rigidity that likely generate interfacial driving forces that propel the motion of cholesterol crystallites.

To test this hypothesis, we employed fluorescence lifetime imaging microscopy (FLIM) to monitor changes in membrane rigidity during cholesterol crystallization on SLBs. As a mechanosensitive probe, we utilized BODIPY-based conjugated oligoelectrolytes (COE-BY) embedded within lipid bilayers (Fig. 4A)[42]. Like other COEs[43–45], COE-BY stably localizes in lipid bilayers and provides consistent emission characteristics over extended periods (up to 48 hours), enabling time-resolved sensing of biophysical changes in membranes. Structurally, COE-BY consists of a conjugated π-electron backbone with hydrophilic and lipophilic substituents that promote membrane insertion (Supplementary Fig. 12A). The excitation and emission maxima of the dye (≈544 nm and ≈580 nm) are compatible with standard FLIM setups (Supplementary Figs. 12B, C). Mechanistically, COE-BY features an environmentally sensitive BODIPY molecular rotor whose fluorescence lifetime responds to lipid packing and membrane rigidity via changes in molecular conformation about its central core[46]. In more tightly packed or mechanically constrained bilayers, intramolecular motion is increasingly hindered, which suppresses non-radiative relaxation pathways and results in longer fluorescence lifetimes[42]. Therefore, the fluorescence lifetime of COE-BY increases with more ordered, rigid lipid packing and decreases with reduced rigidity, making it a mechanosensitive reporter for real-time visualization of dynamic changes in membrane rigidity[42].

FLIM images revealed regions with relatively long amplitude-weighted fluorescence lifetimes (τ_w = ~2 ns, orange and red) at the initial stages during SLB formation and cholesterol crystallite nucleation, as shown in Fig. 4B. Over time, areas with shorter lifetimes (blue) became increasingly evident, indicating a reduction in membrane packing and lipid order during cholesterol crystallization. This observation is corroborated by the average photoluminescence (PL) decay analysis, which showed a progressive decrease in τ_w, with the average dye lifetime dropping from 2.0 ns at 0 min to 1.8 ns at 30 min (Supplementary Fig. 13). We further used phasor analysis as a fitting-independent approach to visualize complex fluorescence decay data[47] (Fig. 4C). At 5.5 min after SLB formation, the lifetime distribution was broad, but over time, it became narrower and converged to a population with shorter lifetimes at 20 min. At 25 min, the previously merged populations dispersed again, indicating ongoing dynamic fluctuations in membrane packing and in the local mechanical environment sensed by COE-BY. The average fluorescence lifetime of COE-BY over time reveals an overall decrease in membrane rigidity, alongside dynamic variations (Fig. 4D). Importantly, COE-BY fluorescence lifetime is interpreted here primarily as a local reporter of molecular packing and mechanical constraint, rather than as a direct measurement of the membrane bending modulus. Recent measurements across phosphatidylcholine–cholesterol membranes demonstrated that bending elasticity depends strongly and nonlinearly on molecular packing[48]. In the same study, an environment-sensitive fluorescence probe showed a corresponding nonlinear relationship between fluorescence lifetime and bending elasticity after probe-specific calibration. Accordingly, comparatively modest changes in the packing-sensitive lifetime may correspond to substantially amplified changes in the membrane bending rigidity. However, a quantitative conversion in the present system would require an independent calibration of COE-BY lifetime against membrane packing and bending elasticity under matched cholesterol-supersaturated supported bilayer conditions.

Taken together, these findings indicate that membrane packing and lipid order decrease during cholesterol crystallization and that these changes are spatially heterogeneous, within the interpretive limits of a packing-sensitive fluorescence probe. The gradual reduction in membrane rigidity is likely due to cholesterol depletion as crystallites nucleate and grow, while the evolving lifetime distributions indicate local remodeling of rigidity fields. Because membrane bending elasticity depends nonlinearly on molecular

https://doi.org/10.1038/s41467-026-79445-1

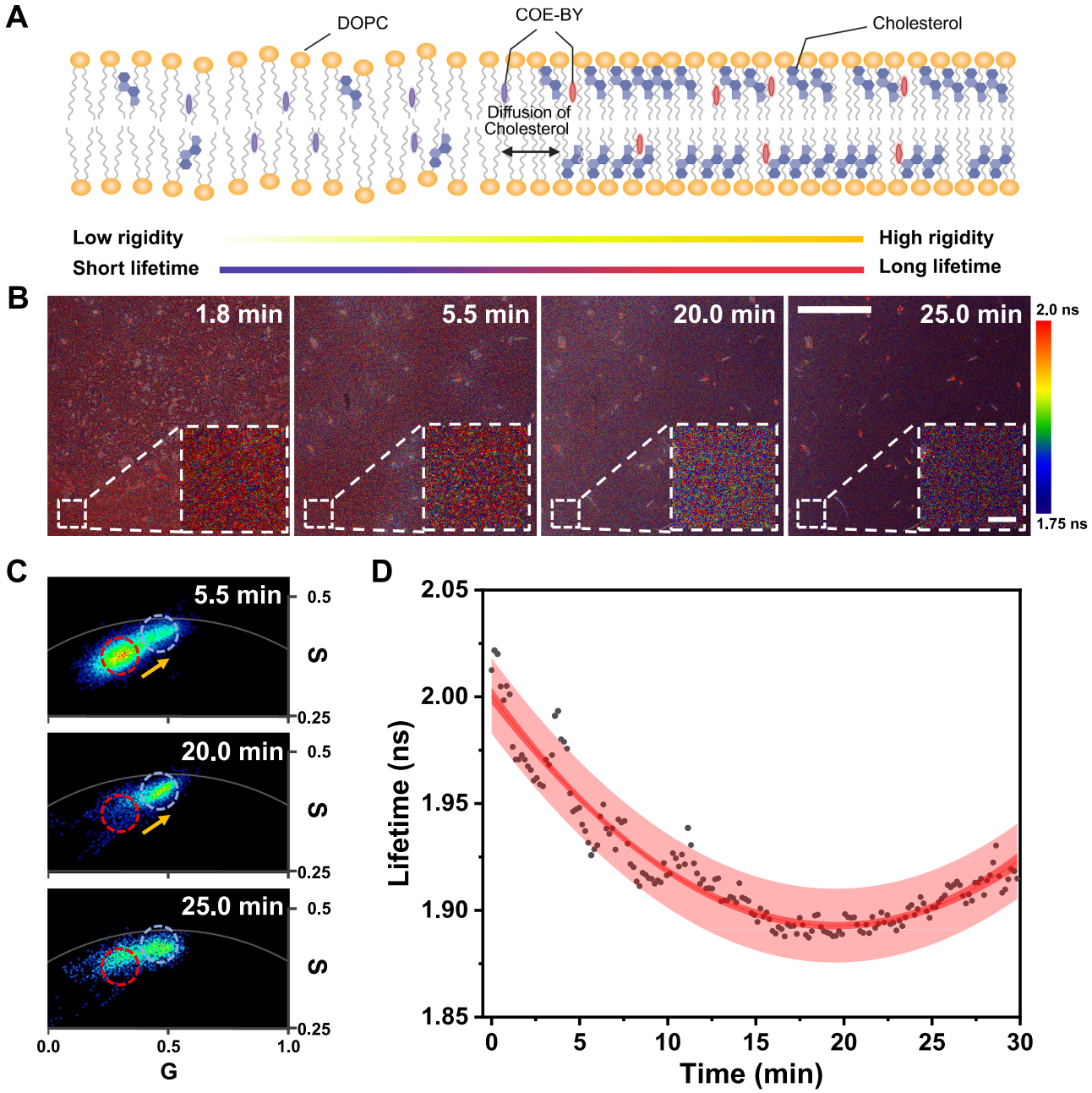

Fig. 4 | Fluorescence lifetime imaging reveals the change in membrane rigidity at DOPC supported lipid membranes accompanying cholesterol crystallite motility. A Schematic illustration depicting the change in membrane rigidity by diffusion and extraction of cholesterol molecules, resulting in a lifetime change of COE-BY, the conjugated oligoelectrolyte serving as a mechanosensitive probe in this experimental setup. Created in BioRender. in Translational Science, E. (2026) https://BioRender.com/fsqu7jf. **B** FLIM maps during the formation of the COE-BY-embedded supported lipid membrane and cholesterol crystallization with motile crystallites; maps are representative of three independent bilayer preparations that gave similar results. Scale bar, 40 µm. Magnified images reveal uniform distribution of COE-BY in the membrane and its progressive lifetime decrease, characterized by a colour change from red to blue. Scale bar, 5 µm. **C** Phasor plots derived from the FLIM images in (**B**) to visualize the relative distribution of emitting species. The population of lifetimes transits from the red circle to the blue circle over time and eventually becomes broadly distributed at 25 min. **D** Time-dependent amplitude-weighted fluorescence lifetime of COE-BY in this system. Individual points represent measured lifetime values. The solid line represents a second-order polynomial fit to the data. The dark and light shaded regions indicate the 95% confidence interval and 95% prediction interval of the fit, respectively. Source data are provided as a Source Data file.

packing[48], these lifetime variations may correspond to a more strongly heterogeneous bending response than would be expected from a conventional interpretation. However, the lifetime measurements do not directly determine the absolute elastic moduli or the magnitude and direction of local rigidity gradients. These findings therefore support, rather than quantitatively establish, a working model in which cholesterol crystallization may generate local rigidity gradients through its interaction with the surrounding membrane, potentially driving the movement of the cholesterol crystallites.

Physical basis of cholesterol crystallite motility

Analogous to cellular haptotaxis or durotaxis, local gradients in membrane rigidity can generate driving forces across the contact region between crystallites and membranes that propel motion (Fig. 5A). Such rigidity gradients can arise as crystallization

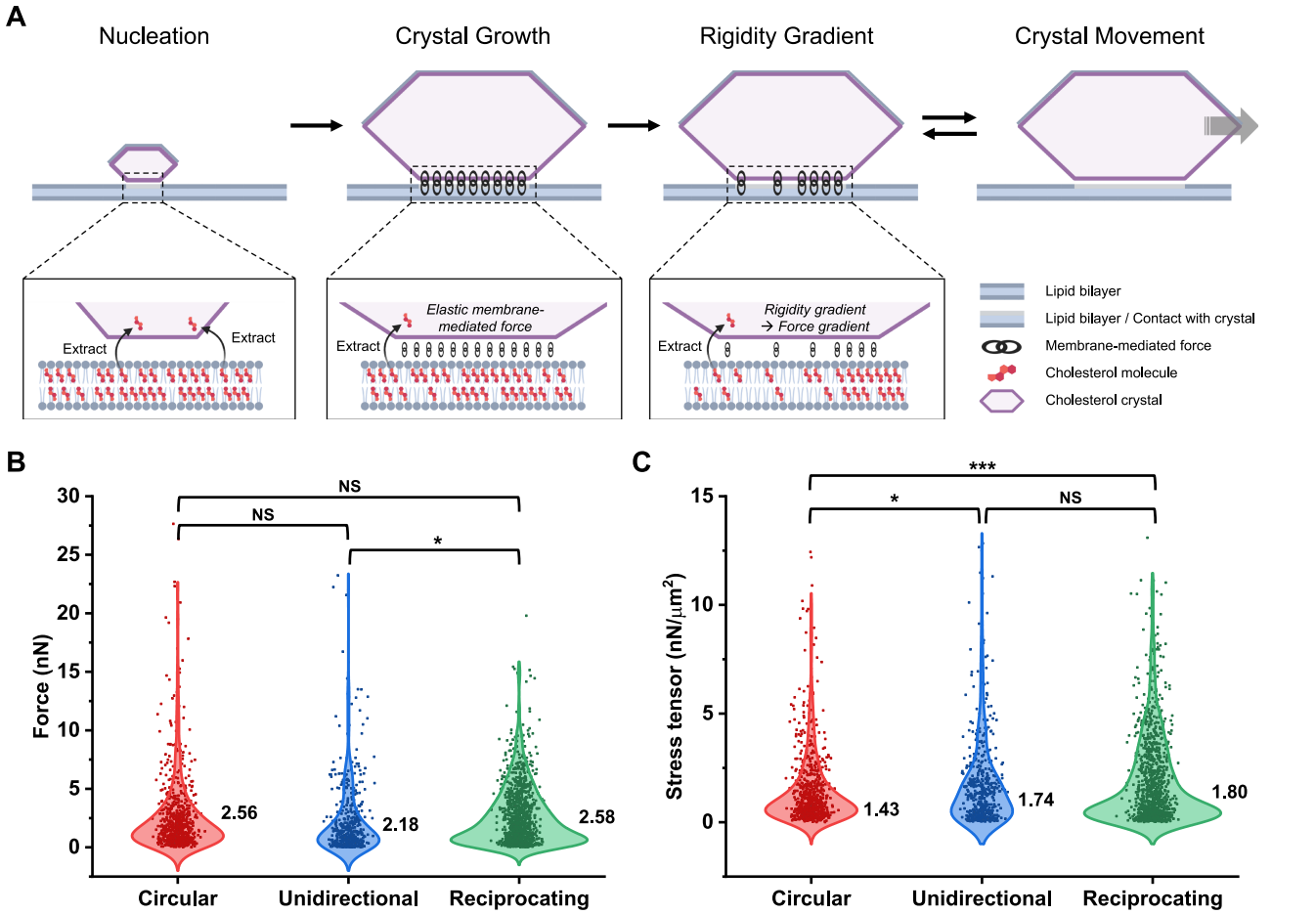

Fig. 5 | Elastic membrane-mediated drivers underlying directional motility of cholesterol crystallites on DOPC supported lipid membranes inferred from mathematical modeling. A Schematic hypothesis suggesting cholesterol-induced rigidity gradients within lipid membranes as a driving force facilitating directional motility of cholesterol crystallites. Created in BioRender. in Translational Science, E. (2026) https://BioRender.com/fsqu7jf. **B**, **C** Distribution of (**B**) inferred driving force and (**C**) stress tensor magnitude acting on crystallites during their motility. Values denote the average force and the average stress tensor trace. Groups were compared using Welch's one-way ANOVA followed by two-sided Games–Howell multiple-comparisons tests, and multiplicity-adjusted *P* values are reported. For the inferred driving force in (**B**): circular versus unidirectional, $P = 0.0987$; circular versus reciprocating, $P = 0.8869$; unidirectional versus reciprocating, $P = 0.0206$. For the stress tensor in (**C**): circular versus unidirectional, $P = 0.01525$; circular versus reciprocating, $P = 0.0000576$; unidirectional versus reciprocating, $P = 0.8495$. $P < 0.05$ was considered statistically significant and asterisks * and *** correspond to P<0.05 and 0.001, respectively, whereas NS indicates no significant difference. Source data are provided as a Source Data file.

locally redistributes and depletes membrane cholesterol, altering lipid packing and mechanics at the crystallite–membrane interface. Even if cholesterol extraction is locally uniform at the crystallite–membrane interface, finite lateral diffusion in supported bilayers prevents instantaneous relaxation of cholesterol depletion patterns[49]. Once motion begins, the crystallite effectively behaves as a moving sink, encountering relatively less-depleted membrane ahead while leaving a depletion wake behind, which sustains a rigidity asymmetry during continuous motion. This feedback-based symmetry breaking is conceptually consistent with self-phoretic and Marangoni-type propulsion frameworks in which persistent gradients emerge from coupled interfacial activity and transport rather than an imposed directional cue[50,51].

To quantify these driving forces, we developed a mathematical framework to calculate the forces and 2D stress tensor trace. This approach builds on the free draining model, previously used for diffusion and drift of nanoparticles mediated by multivalent interactions with a SLB (e.g., lipid vesicles attached via cholesterol-based DNA linkers)[37]. The transient motility of cholesterol crystallites on lipid bilayers represents a specialized case of this model. In this framework, the diffusion coefficient of cholesterol crystallites, D, is expressed as,

$$D = D_* / n, \tag{1}$$

where D_* is the diffusion coefficient of a single cholesterol molecule, assumed to be 2 μm²/s based on the literature[52], and n is the number of cholesterol molecules at the contact area between the crystallite and the lipid bilayer. Here, D_* denotes the lateral diffusion coefficient of a cholesterol molecule in the membrane plane adjacent to the crystallite–membrane contact, rather than diffusion of the micrometer-scale crystallite or of cholesterol within the crystalline phase. Parameter n is estimated as,

$$n = S / s, \tag{2}$$

where S is the contact area between the crystallite and the lipid bilayer, and s is the contact area per cholesterol molecule, assumed to be 0.223 nm² based on the literature[53]. It is important to note that n may be overestimated since not all molecules within the contact region are linked to the lipid bilayer. The time-dependent S for each crystallite (see Fig. 3C and Supplementary Fig. 9) allows us to calculate the corresponding time-dependent D using Eqs. (1) and (2). Additionally,

the drift velocity, v, under the influence of an external force, F, is given by,

$$v = \alpha F, \tag{3}$$

where α, the motility related to the diffusion coefficient as

$$\alpha = D/k_B T, \tag{4}$$

where k_B is the Boltzmann constant, and T is the absolute temperature.

With the specification above, the time-dependent F was calculated for each moving crystallite (Supplementary Fig. 14A–C), and continuous F distributions are presented for each motion type (Fig. 5B). The calculated average forces during crystallite movement were ≈2.56 nN for circular motion, ≈2.18 nN for unidirectional motion, and ≈2.58 nN for reciprocating motion. These values represent effective net interfacial forces integrated over the finite crystallite–membrane contact region, rather than molecular-scale point forces or direct mechanical measurements. In conjunction with the ranks in Fig. 3E, F (velocity: unidirectional ≥ reciprocating > circular; fold-change in contact area: unidirectional ≥ reciprocating > circular), these results suggest that path geometry and resistive coupling, rather than force magnitude alone, set translation. Circular and reciprocating trajectories reorient frequently and experience stronger resistive coupling at the contact, resulting in lower velocities despite stronger forces, whereas unidirectional trajectories maintained straighter, more efficient paths and therefore achieved the highest velocity with lower forces. Notably, the calculated forces (≈2–3 nN) are substantially higher than those typically observed in dynamic membrane processes, such as single-molecule transport (~70 pN)[54]. These forces are comparable to forces reported to mechanically perturb lipid membranes (~0.5–3 nN)[55,56] and even sufficient to disrupt or rupture the membrane (~1–10 nN)[57], highlighting the mechanical impact of steep membrane rigidity gradients.

Phenomenologically, the driving force F can be represented as (cf. the equations for diffusion of impurities in solids[58])

$$F \approx S\nabla\sigma_{ii}/2, \tag{5}$$

where σ_{ii} is the trace of the 2D stress tensor. With the specification above, the time-dependent changes in $\nabla\sigma_{ii}$ were calculated for each moving crystallite (Supplementary Figs. 14D-F). From this relationship, we estimated σ_{ii} distributions for each motion type (Fig. 5C). The calculated average σ_{ii} values during crystallite movement were ≈ 1.43 nN/μm^2, ≈1.74 nN/μm^2, and ≈1.80 nN/μm^2 for circular, unidirectional, and reciprocating motion, respectively. The mean stress ordering (reciprocating ≈ unidirectional > circular) differs from the force ordering (circular ≈ reciprocating > unidirectional), because contact area S varies systematically across types (typically larger for circular and smaller for unidirectional; see Supplementary Fig. 9). Consequently, unidirectional trajectories attain larger per-area gradients over small contacts and thus translate straighter and faster at modest forces. Conversely, circular trajectories integrate shallower gradients over larger contacts with frequent reorientation, yielding lower velocity despite larger forces. Reciprocating trajectories lie between, with high forces and gradients that can alternate in direction, consistent with heading reversals. Interestingly, the inferred stress values fall within biologically relevant ranges, including contractile forces in cardiomyocytes (2–5 nN/μm^2)[59], focal adhesions during cell-matrix adhesion in myofibroblasts (3.8 ± 5.1 nN/μm^2)[60], and traction forces of keratocytes (0.2–0.4 nN/μm^2)[61], situating this interfacial transport in a physiological mechanical regime.

Of note, σ_{ii} values reported here were inferred metrics rather than direct mechanical measurements. While circular motion showed statistically distinguishable σ_{ii} values compared to the other motions, their absolute magnitudes are modest. These modest differences should not, however, be interpreted as equivalently modest differences in the local mechanical fields associated with motion. The reported stress values are effective, time-resolved scalar quantities inferred using the apparent contact area and averaged over the motility interval, thus they do not spatially resolve the hypothesized leading-to-trailing asymmetry at the crystallite–membrane interface. Moreover, the nonlinear relationship between molecular packing and bending elasticity implies that small packing differences may produce larger differences in local bending response and consequently, in the energetic cost of membrane deformation[48]. Pronounced differences in trajectory may therefore arise from the spatial distribution, orientation, and temporal evolution of the mechanical field, rather than from large differences in its mean scalar magnitude alone. Future studies combining direct mechanical calibration with expanded datasets will be important to quantify sensitivity and establish a robust mechanistic relationship between interfacial stress gradients and motility mode selection.

Crystallite morphology may also modulate how a non-equilibrium interfacial field is converted into motion. An elongated contact footprint introduces anisotropic translational resistance and may favor motion along its long axis when the resultant interfacial force is approximately aligned with that axis and passes near the center of interfacial resistance. By contrast, a curved or asymmetric footprint may produce an offset between the resultant force and the center of resistance, thereby generating a rotational moment and favoring reorientation or circular motion. Reciprocating motion is unlikely to arise from static morphology alone and may instead require temporal reversals in the polarity or spatial distribution of the interfacial driving field. Nevertheless, quantitative analysis revealed substantial overlap in aspect ratio and solidity among all three trajectory classes (see Supplementary Fig. 11), demonstrating that morphology alone is insufficient to determine motion mode. In addition, the present free-draining model does not explicitly resolve shape-dependent translational resistance or rotational torque. Instead, crystallite geometry, membrane deformation, adhesion, interfacial friction, and fluid and membrane drag are coarse-grained into an effective scalar mobility. The inferred force and stress values therefore permit comparative analysis of interfacial driving but do not independently predict trajectory mode. A fully shape-resolved model would require three-dimensional crystallite geometry and spatially resolved interfacial-force measurements that are beyond the resolution of the present experiments.

Design guidance for cholesterol crystallite transport

Building on the force-stress framework, we asked whether the membrane state can tune the motility of cholesterol crystallites. We prepared SLBs spanning fluidic DOPC to rigid 1,2-dipalmitoyl-sn-glycero-3-phosphocholine (DPPC) lipid compositions by applying cholesterol-supersaturated bicellar mixtures of DOPC, DOPC/DPPC (50/50 mol%), and DPPC. These three lipid compositions span well-established differences in intrinsic mechanical properties. In cholesterol-free bilayers, reported literature values indicate bending stiffness (k_c) of ~18 k_BT for DOPC and ~57 k_BT for DPPC, and area stretch modulus (k_A) of ~106 pN/nm and ~199 pN/nm, respectively[62,63]. These established values define a quantitative mechanical hierarchy in which DOPC membranes are substantially more compliant than DPPC membranes, with mixed DOPC/DPPC systems expected to exhibit intermediate properties. Of note, these literature values are used only to establish the relative mechanical distinction between the underlying phospholipid matrices and should not be interpreted as the absolute elastic moduli of the dynamically evolving, cholesterol-supersaturated supported bilayers employed here. Although our supported bilayers are cholesterol-

https://doi.org/10.1038/s41467-026-79445-1

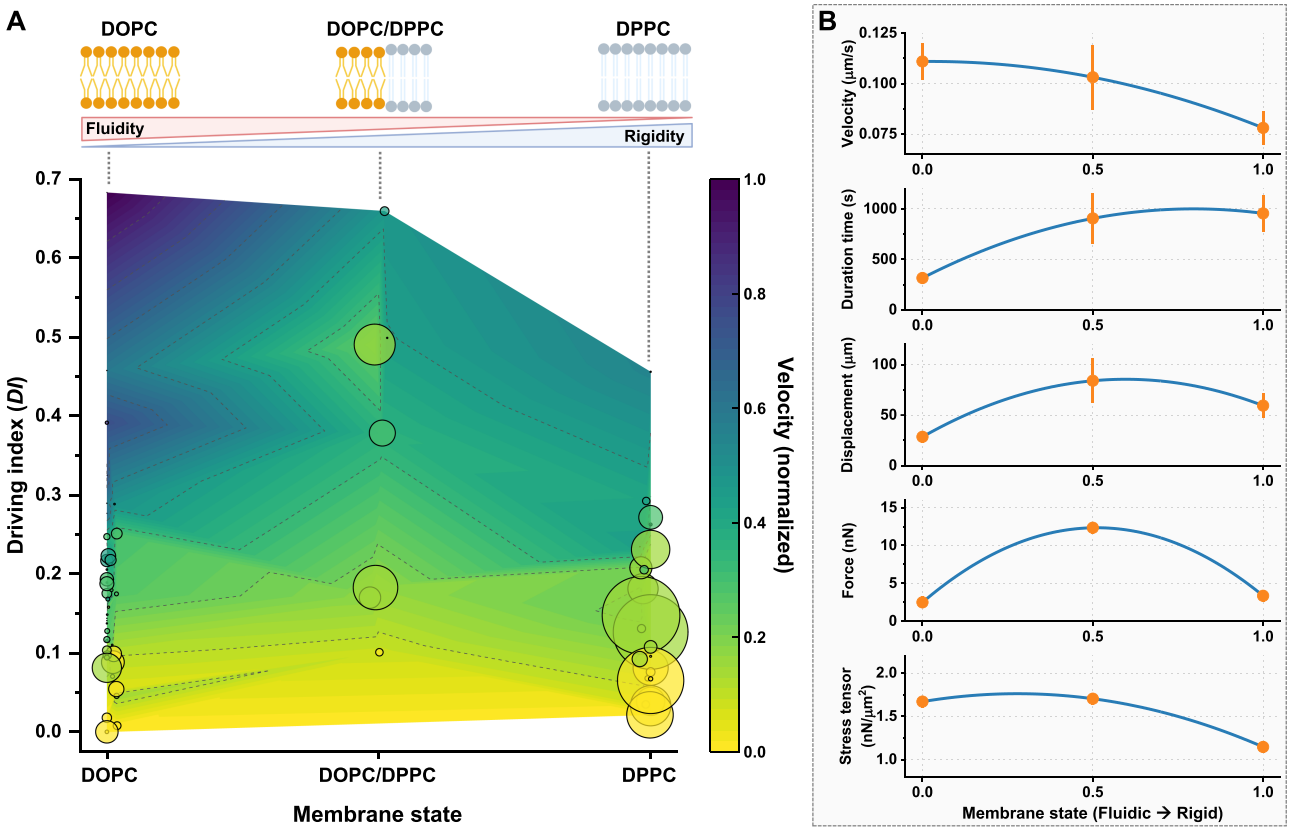

Fig. 6 | Quantitative design guidance for directional motility of cholesterol crystallites. A Operating map relating membrane state (fluidic to rigid, tuned by lipid composition) to motility outputs. The top schematic aligns lipid composition with the x axis: DOPC, fluidic membrane; DOPC/DPPC, mixed; DPPC, rigid membrane, and is an original illustration prepared by the authors using BioRender.com. The background colour shows the model-derived normalized velocity as a function of membrane state and the driving index DI (min-max normalization within the dataset). Each circle represents an individual track of a single crystallite, with colour encoding the measured velocity and size encoding the motility duration. Created in BioRender. in Translational Science, E. (2026) https://BioRender.com/fsqu7jf. **B** Membrane state-wise trends for velocity, duration, displacement, inferred driving force and stress tensor. Data are presented as mean values ± s.e.m. In (**A**, **B**), $n = 46$ (DOPC), $n = 7$ (DOPC/DPPC) and $n = 25$ (DPPC) individual motile crystallites, each pooled from three independent supported lipid bilayer preparations; the unit of study is a single tracked crystallite (see Supplementary Fig. 15). Source data are provided as a Source Data file.

supersaturated during crystallization, progressive cholesterol extraction into growing crystallites shifts the membrane toward mechanical behavior governed increasingly by the underlying phospholipid matrix. Across these mechanically distinct membrane states, the prevalence of motile cholesterol crystallites depended on lipid composition (Supplementary Fig. 15). Although all three motion types appear under DOPC/DPPC and DPPC conditions, events were rarer in the mixed state. Representative microscopic images of cholesterol crystallization and all tracked crystallites for each state are shown in Supplementary Figs. 16, 17 (DOPC: $n = 46$, DOPC/DPPC: $n = 7$, DPPC: $n = 25$).

By tuning membrane state from fluid to rigid, we constructed a quantitative operating map, defined as a data-driven design chart that relates membrane state (lipid composition) to motility outputs (e.g., velocity, duration, displacement) using single particle tracking coupled to mathematical modeling (Fig. 6A). This operating map provides empirical design guidance for controlling cholesterol crystallite transport on lipid interfaces within the compositional range examined here. To collapse force and stress contributions into a single parameter, we defined a dimensionless driving index, DI, as

$$\mathrm{DI} = \sqrt{norm(F)} * \sqrt{norm(\sigma_{ii})}, \quad (6)$$

where norm(·) denotes min–max normalization to [0,1] across the dataset for each quantity. Point color encodes normalized velocity and point size encodes motility duration. Within each composition, DI is associated with velocity, linking rigidity-derived drivers (force and stress) to transport output.

Detailed motility trends across membrane states are shown in Fig. 6B. Velocity decreased monotonically with increasing membrane rigidity. This trend was associated with contact area, which increases on more rigid membranes, spreading the available driving over a wider interface and increasing dissipation (Supplementary Fig. 18A). Duration increased with membrane rigidity, but total displacement peaked at the mixed DOPC/DPPC state where intermediate velocity coincides with long motility (Supplementary Fig. 18B). Notably, although micron-scale phase separation was not apparent in fluorescence micrographs under the cholesterol-supersaturated crystallization conditions in supported bilayer, the DOPC/DPPC membrane can nonetheless exhibit nanoscale lateral heterogeneity and local packing substructure that are below optical resolution. Such nanoscopic heterogeneity is consistent with prior work showing that Lo/Ld organization and internal substructure can occur on length scales that vary widely with composition and need not yield optically resolvable domains[64,65]. However, the DOPC/DPPC condition does not directly address sphingomyelin/cholesterol-rich ordered domains, which involve distinct molecular interactions and phase behavior in cellular membranes[64,66]. Within this, mixed membranes access higher DI regimes, plausibly reflecting enhanced force transmission arising from compositional boundaries, whereas the stress readout likewise showed a shallow maximum in the mixed state and declined on rigid DPPC (Supplementary Fig. 18C).

In summary, the operating map indicates that fluidic lipid membranes support fast but short runs, rigid lipid membranes show slow but long runs, and mixed membranes maximize total displacement. In practice, one can choose lipid composition to place the system in a target DI-band that delivers the desired velocity–duration pair to meet a required displacement. To explore active control of motility, we further leveraged methyl-β-cyclodextrin (MβCD), a catalyzing molecule for cholesterol transfer (Supplementary Fig. 19). The addition of MβCD after motion arrest reactivated motion, suggesting renewed cholesterol exchange that may help rebuild rigidity gradients and return the system to a non-equilibrium crystallization regime conducive to motility. Notably, FLIM analysis revealed a time-dependent decrease in fluorescence lifetime of COE-BY after MβCD addition, consistent with cholesterol depletion-driven mechanical remodeling of the membrane (Supplementary Fig. 20). Because bending elasticity depends nonlinearly on molecular packing[48], the associated change in mechanical response may be larger than the lifetime shift alone suggests. MβCD-mediated cholesterol transfer may therefore contribute to motion reactivation by restoring cholesterol flux and regenerating a packing asymmetry at the crystallite–membrane interface whose mechanical consequences may be amplified by the nonlinear packing-elasticity relationship. Nevertheless, without a COE-BY-specific mechanical calibration, these measurements are interpreted as evidence of packing remodeling rather than as a direct quantitative measurement of bending-modulus change. Prior studies have also shown that cyclodextrin-mediated cholesterol depletion can measurably remodel membrane mechanical properties in model systems, supporting the premise that cholesterol exchange can shift membrane mechanics[67]. Together, the operating map and MβCD-mediated motion reactivation demonstrate composition-dependent and on-demand modulation of crystallite transport under the conditions examined here.

Discussion

This study reports directional, self-propelled motion of cholesterol crystallites on phospholipid membranes. These observations support a working model in which local cholesterol redistribution generates heterogeneous membrane packing and mechanical asymmetry associated with local rigidity gradients, establishing a physical feedback loop between crystallite growth and bilayer mechanics. The combination of real-time fluorescence imaging, single particle tracking, FLIM analysis, and mechanical modeling supports the role of rigidity-mediated propulsion mechanisms such as haptotaxis and durotaxis in guiding crystallite motility, although the absolute local elastic moduli and rigidity gradients remain to be directly quantified. Membrane-state modulation yielded an empirical map relating composition to motility, providing design guidance for tuning transport on lipid interfaces within the compositional range examined here.

An important limitation of the present study is that the cholesterol-supersaturated supported bilayers were designed to isolate the physical coupling between cholesterol crystallization, membrane remodeling, and motility rather than to reproduce the full complexity of cellular membranes. The potentially general feature revealed by this model system is the non-equilibrium feedback through which growth of a cholesterol-rich crystallizing phase redistributes membrane cholesterol and alters the surrounding packing and mechanical environment. However, the onset, magnitude, persistence, and trajectory of motion are likely to depend on membrane composition, cholesterol accessibility, lateral transport, substrate coupling, and interfacial resistance. In particular, the DOPC/DPPC membranes examined here do not directly reproduce the molecular organization of sphingomyelin/cholesterol-rich environments, which exhibit composition-dependent Lo/Ld phase behavior[66]. In cellular plasma membrane, cholesterol is also partitioned into pools with differing accessibility, including a sphingomyelin-sequestered pool[68], and accessible cholesterol is actively regulated through non-vesicular transport pathways such as Aster-mediated transport to the endoplasmic reticulum[69]. These mechanisms may buffer or spatially redistribute cholesterol and could therefore suppress, localize, or modify the proposed rigidity gradients. Accordingly, the present study does not demonstrate that the distribution of crystallite motility modes observed here is necessarily reproduced in living cells. Future studies using phase-separated sphingomyelin-containing membranes and cell-derived systems such as giant plasma membrane vesicles[70] will be important for determining how native membrane organization modifies cholesterol crystallization-driven remodeling and motility.

Although identical directional motion has not been established in vivo, the crystallization–membrane feedback loops may become relevant in pathological environments where local cholesterol-buffering and transport mechanisms are exceeded and cholesterol-rich crystalline phases are formed. In atherosclerosis, for example, local cholesterol crystallization within arterial walls may remodel nearby lipid-rich interfaces and generate mechanical perturbations, although whether directional crystallite motion or a related feedback mechanism contributes to plaque remodeling or instability remains to be determined directly. More broadly, harnessing crystallization-induced rigidity gradients opens opportunities for engineering synthetic lipid systems. By strategically controlling crystallization processes within membranes, such as tuning lipid composition or catalyzing cholesterol transfer, it may become possible to design self-organizing, force-generating lipid platforms capable of dynamic remodeling, cargo transport, or pattern formation, with applications in biomimetic materials and soft robotics. Future efforts may expand this framework to other crystallizable molecules and programmable membrane compositions, facilitating the rational design of responsive, transport-capable lipid interfaces.

Methods

Reagents

1,2-Dioleoyl-sn-glycero-3-phosphocholine (DOPC), 1,2-dipalmitoyl-sn-glycero-3-phosphocholine (DPPC), 1,2-dihexanoyl-sn-glycero-3-phosphocholine (DHPC) and 1,2-dipalmitoyl-sn-glycero-3-phosphoethanolamine-N-(lissamine rhodamine B sulfonyl) (ammonium salt) (Rh-PE) lipids, each dissolved in chloroform, as well as cholesterol powder, were purchased from Avanti Polar Lipids (Alabaster, AL). The excitation/emission spectra of COE-BY were acquired using a UV-3600i spectrophotometer (Shimadzu Corp., Kyoto, Japan) with standard 10 × 10 mm quartz cuvettes. Photoluminescence (PL) spectra were measured on a Fluorolog-3 spectrofluorometer (Horiba Scientific, Kyoto, Japan) equipped with an R13456 photomultiplier tube (PMT) detector. Methyl-β-cyclodextrin (MβCD) was purchased from Cyclo-Lab (Budapest, Hungary). All buffer solutions used throughout the experiments consisted of 10 mM Tris and 150 mM NaCl at pH 7.5, prepared using Milli-Q-treated water (Millipore Sigma, Burlington, MA).

Preparation of Bicellar Mixtures

To prepare bicelle samples, a mixture of long-chain phospholipids (i.e. DOPC, DPPC) and cholesterol was combined at a molar ratio of 20:80 (mol% of total long-chain lipids), along with DHPC, in a glass vial. The solvent was removed by a gentle stream of nitrogen gas, resulting in the formation of a dry lipid film. For fluorescence imaging, Rh-PE and/or COE-BY were incorporated at 0.5 mol% relative to total long-chain phospholipids. The dried film was placed under vacuum overnight. Hydration was then carried out with 10 mM Tris, 150 mM NaCl buffer (pH 7.5) to achieve a final molar ratio (q) of 0.25 (i.e., 1 mM long-chain lipid and 4 mM DHPC). The lipid suspension underwent five freeze–thaw–vortex cycles, which included: (1) immersion in liquid nitrogen for 1 min, (2) thawing in a 60 °C water bath for 5 min, and (3) vortexing for 30 s. Just before use, the lipid mixture was diluted 32-

fold with buffer solution, yielding final concentrations of 0.031 mM for long-chain phospholipids/cholesterol and 0.125 mM for DHPC.

Epifluorescence microscopy

Fluorescence imaging was performed using a Nikon Eclipse Ti-E inverted microscope equipped with a 60× oil-immersion objective lens (NA 1.49). Illumination was provided by a C-HGFIE Intensilight mercury-fiber lamp (Nikon, Tokyo, Japan), and the light was passed through a dichroic filter block (excitation 545/30 nm, emission 605/70 nm). Images were recorded with an iXon3 897 EMCCD camera (Andor, Belfast, UK) at a rate of one frame per 3 seconds. Glass coverslips (ibidi GmbH, Martinsried, Germany) were cleaned with 1% (w/v) sodium dodecyl sulfate (SDS), deionized water, and 95% ethanol, followed by drying under nitrogen gas. To enhance hydrophilicity, the glass surface was treated with oxygen plasma for 1 minute using a PDC-002 plasma cleaner (Harrick Plasma, Ithaca, NY). Cleaned coverslips were assembled in an ibidi sticky-Slide VI 0.4 microfluidic chamber, and lipid suspensions were injected at a flow rate of 100 µL/min for 5 min, controlled by a Reglo Digital peristaltic pump (ISM833C, Ismatec, Wertheim, Germany), then the flow was stopped. To demonstrate that bulk convective flow was negligible, an approximately 50 nm fluorescent tracer vesicle in the supernatant was monitored for 15 min under the same static imaging conditions used for crystallite-motility measurements. The tracer position was tracked frame-by-frame using ImageJ. The resulting trajectory is shown in Supplementary Fig. 21. All imaging was carried out at room temperature (~ 25 °C).

Fluorescence Lifetime Imaging Microscopy (FLIM)

FLIM measurements were performed on a SP8 DIVE Deep In Vivo Explorer confocal microscope (Leica, Wetzlar, Germany) equipped with a 63× water-immersion objective, using time-correlated single photon counting (TCSPC) methodology. Image acquisition and analysis were carried out using LAS X software[43,45]. Phasor analysis was conducted by applying a Fourier transform to the time-domain data for each pixel, generating a model-free representation of lifetime distributions. In this approach, the Fourier transform of each fluorescence decay is represented in a 2D plot using its cosine (G) and sine (S) components. Each point on the phasor plot represents a single fluorescence decay event recorded through FLIM. Points located to the left of the horizontal axis are associated with longer fluorescence lifetimes. Global biexponential fitting was used to calculate the fluorescence lifetime of COE-BY, with analysis restricted to pixels containing a minimum of 200 photons. Image acquisition was set to ≤1 photon per pulse. The amplitude-weighted fluorescence lifetime (τ_w) was calculated as[45]:

$$\tau_w = \sum_{i=1}^{p} A_i \tau_i / \sum_{i=1}^{p} A_i$$

Spectrally-resolved images were collected at 10 nm steps across a 400–800 nm wavelength range under excitation at 1090 nm.

Single particle tracking of cholesterol crystallite dynamics

Cholesterol crystallite velocities were analyzed in Fiji (ImageJ v1.54 f). Trajectories of individual moving crystallites were traced using the TrackMate plugin (v7.11.1) in Fiji. Corresponding contact areas between cholesterol crystallites and SLBs were determined by manually measuring crystallite dimensions in ImageJ.

Quantitative operating map construction

For each motile crystallite, trajectories were obtained using TrackMate plugin in Fiji and corresponding contact area was quantified from fluorescence images. Time-dependent inferred driving force and stress tensor were computed from measured contact area and velocity using Eqs. (1–5). Track-level mean values were obtained by averaging metric over the motility window for each crystallite. To generate a single design axis, we defined a dimensionless driving index (DI) using Eq. (6) by min-max normalizing each track-averaged driving metric across the full dataset to the range [0, 1]. The operating map plots individual tracks in the space of membrane state versus DI, with mean velocity and duration encoded as point color and size, respectively.

Cyclodextrin treatment for motion reactivation

For motion reactivation, 1 mM MβCD was prepared fresh in buffer (10 mM Tris, 150 mM NaCl, pH 7.5). After cholesterol crystallites had become stationary under no-flow conditions on DOPC SLBs, MβCD solution was introduced into the microfluidic channel at 100 µL/min. Reactivated crystallites were tracked by the TrackMate plugin in Fiji using the same detection and linking parameters as baseline analyses. All experiments were carried out at room temperature (~ 25 °C).

Statistical analysis

Data were analyzed using Welch's one-way analysis of variance (ANOVA), followed by two-sided Games–Howell multiple-comparisons tests. The Games–Howell procedure was used because it does not assume equal variances or equal sample sizes among groups. Multiplicity-adjusted P values are reported for each post hoc pairwise comparison, with exact P values provided in the corresponding figure legends and Source Data file. $P < 0.05$ was considered statistically significant, and significance is indicated as $^{*}P < 0.05$, $^{**}P < 0.01$ and $^{***}P < 0.001$. No statistical method was used to predetermine sample size. Sample sizes correspond to the number of individual motile crystallites that could be unambiguously detected and tracked across three independent supported lipid bilayer preparations for each membrane composition, and every crystallite meeting the detection and tracking criteria was included. The experiments were not randomized, and the investigators were not blinded to conditions during acquisition or analysis. All quantitative measurements were evaluated using the same prespecified tracking and measurement procedures across groups. Statistical analyses were performed in OriginPro 2024.

Reporting summary

Further information on research design is available in the Nature Portfolio Reporting Summary linked to this article.

Data availability

All data supporting the findings of this study are available within the article and its Supplementary Information file. The source data underlying Figs. 2A, B, 3C–F, 4D, 5B, C, 6A, and B and Supplementary Figs. 4B, 9, 10, 11, 13, 14, 15, 18, 19B, and 20B are provided as a Source Data file. Representative microscopy images and trajectory visualizations are provided in the article and Supplementary Information. Source data are provided with this paper.

References

1. Addadi, L. & Weiner, S. Control and design principles in biological mineralization. *Angew. Chem. Int. Ed. Engl.* **31**, 153–169 (1992).
2. Archibald, D. D. & Mann, S. Template mineralization of self-assembled anisotropic lipid microstructures. *Nature* **364**, 430–433 (1993).
3. Firouzi, A. et al. Cooperative organization of inorganic-surfactant and biomimetic assemblies. *Science* **267**, 1138–1143 (1995).
4. Bach, D. & Wachtel, E. Phospholipid/cholesterol model membranes: formation of cholesterol crystallites. *Biochim. Biophys. Acta Biomembr.* **1610**, 187–197 (2003).
5. Ziblat, R., Fargion, I., Leiserowitz, L. & Addadi, L. Spontaneous formation of two-dimensional and three-dimensional cholesterol

crystals in single hydrated lipid bilayers. *Biophys. J.* **103**, 255–264 (2012).
6. Duewell, P. et al. NLRP3 inflammasomes are required for atherogenesis and activated by cholesterol crystals. *Nature* **464**, 1357–1361 (2010).
7. Varsano, N. et al. Two polymorphic cholesterol monohydrate crystal structures form in macrophage culture models of atherosclerosis. *Proc. Natl. Acad. Sci. USA* **115**, 7662–7669 (2018).
8. Sedaghat, A. & Grundy, S. M. Cholesterol crystals and the formation of cholesterol gallstones. *N. Engl. J. Med.* **302**, 1274–1277 (1980).
9. Pang, C. E., Messinger, J. D., Zanzottera, E. C., Freund, K. B. & Curcio, C. A. The onion sign in neovascular age-related macular degeneration represents cholesterol crystals. *Ophthalmology* **122**, 2316–2326 (2015).
10. Huang, J., Buboltz, J. T. & Feigenson, G. W. Maximum solubility of cholesterol in phosphatidylcholine and phosphatidylethanolamine bilayers. *Biochim. Biophys. Acta Biomembr.* **1417**, 89–100 (1999).
11. Nielsen, M. H., Aloni, S. & De Yoreo, J. J. In situ TEM imaging of $CaCO_3$ nucleation reveals coexistence of direct and indirect pathways. *Science* **345**, 1158–1162 (2014).
12. Ziblat, R., Kjaer, K., Leiserowitz, L. & Addadi, L. Structure of cholesterol/lipid ordered domains in monolayers and single hydrated bilayers. *Angew. Chem. Int. Ed.* **48**, 8958–8961 (2009).
13. Ziblat, R., Leiserowitz, L. & Addadi, L. Crystalline domain structure and cholesterol crystal nucleation in single hydrated DPPC:cholesterol:POPC bilayers. *J. Am. Chem. Soc.* **132**, 9920–9927 (2010).
14. Ziblat, R., Leiserowitz, L. & Addadi, L. Crystalline lipid domains: characterization by X-ray diffraction and their relation to biology. *Angew. Chem. Int. Ed.* **50**, 3620–3629 (2011).
15. Solomonov, I., Weygand, M. J., Kjaer, K., Rapaport, H. & Leiserowitz, L. Trapping crystal nucleation of cholesterol monohydrate: relevance to pathological crystallization. *Biophys. J.* **88**, 1809–1817 (2005).
16. Varsano, N., Fargion, I., Wolf, S. G., Leiserowitz, L. & Addadi, L. Formation of 3D cholesterol crystals from 2D nucleation sites in lipid bilayer membranes: implications for atherosclerosis. *J. Am. Chem. Soc.* **137**, 1601–1607 (2015).
17. Varsano, N. et al. The effect of the phospholipid bilayer environment on cholesterol crystal polymorphism. *ChemPlusChem* **84**, 338–344 (2019).
18. Park, S., Sut, T. N., Ma, G. J., Parikh, A. N. & Cho, N.-J. Crystallization of cholesterol in phospholipid membranes follows Ostwald's rule of stages. *J. Am. Chem. Soc.* **142**, 21872–21882 (2020).
19. Chakraborty, D. et al. Direct observation of cholesterol monohydrate crystallization. *Proc. Natl. Acad. Sci. USA* **122**, e2415719122 (2025).
20. Wang, H. H., Portincasa, P., Liu, M. & Wang, D. Q.-H. Effects of biliary phospholipids on cholesterol crystallization and growth in gallstone formation. *Adv. Ther.* **40**, 743–768 (2023).
21. Epand, R. M., Bach, D., Borochov, N. & Wachtel, E. Cholesterol crystalline polymorphism and the solubility of cholesterol in phosphatidylserine. *Biophys. J.* **78**, 866–873 (2000).
22. Mason, R. P., Tulenko, T. N. & Jacob, R. F. Direct evidence for cholesterol crystalline domains in biological membranes: role in human pathobiology. *Biochim. Biophys. Acta Biomembr.* **1610**, 198–207 (2003).
23. Mainali, L., Raguz, M. & Subczynski, W. K. Formation of cholesterol bilayer domains precedes formation of cholesterol crystals in cholesterol/dimyristoylphosphatidylcholine membranes: EPR and DSC studies. *J. Phys. Chem. B* **117**, 8994–9003 (2013).
24. Alfano, C. et al. Molecular crowding: the history and development of a scientific paradigm. *Chem. Rev.* **124**, 3186–3219 (2024).
25. Raucher, D. & Sheetz, M. P. Cell spreading and lamellipodial extension rate is regulated by membrane tension. *J. Cell Biol.* **148**, 127–136 (2000).
26. Devreotes, P. N. et al. Excitable signal transduction networks in directed cell migration. *Annu. Rev. Cell Dev. Biol.* **33**, 103–125 (2017).
27. Schuh, M. An actin-dependent mechanism for long-range vesicle transport. *Nat. Cell Biol.* **13**, 1431–1436 (2011).
28. Ji, C. & Huang, Y. Durotaxis and negative durotaxis: where should cells go? *Commun. Biol.* **6**, 1169 (2023).
29. Carter, S. B. Haptotaxis and the mechanism of cell motility. *Nature* **213**, 256–260 (1967).
30. Sut, T. N., Park, S., Choe, Y. & Cho, N.-J. Characterizing the supported lipid membrane formation from cholesterol-rich bicelles. *Langmuir* **35**, 15063–15070 (2019).
31. Kolahdouzan, K. et al. Optimizing the formation of supported lipid bilayers from bicellar mixtures. *Langmuir* **33**, 5052–5064 (2017).
32. Tae, H., Park, S., Ma, G. J. & Cho, N.-J. Nanoarchitectured air-stable supported lipid bilayer incorporating sucrose–bicelle complex system. *Nano Converg.* **9**, 3 (2022).
33. Ma, G. J., Zhdanov, V. P., Park, S., Sut, T. N. & Cho, N.-J. Mechanistic aspects of the evolution of 3D cholesterol crystallites in a supported lipid membrane via a quartz crystal microbalance with dissipation monitoring. *Langmuir* **37**, 4562–4570 (2021).
34. Craven, B. M. Crystal structure of cholesterol monohydrate. *Nature* **260**, 727–729 (1976).
35. Crane, J. M. & Tamm, L. K. Role of cholesterol in the formation and nature of lipid rafts in planar and spherical model membranes. *Biophys. J.* **86**, 2965–2979 (2004).
36. Tinevez, J.-Y. et al. TrackMate: an open and extensible platform for single-particle tracking. *Methods* **115**, 80–90 (2017).
37. Block, S., Zhdanov, V. P. & Höök, F. Quantification of multivalent interactions by tracking single biological nanoparticle mobility on a lipid membrane. *Nano Lett.* **16**, 4382–4390 (2016).
38. Solon, J., Streicher, P., Richter, R., Brochard-Wyart, F. & Bassereau, P. Vesicles surfing on a lipid bilayer: self-induced haptotactic motion. *Proc. Natl. Acad. Sci. USA* **103**, 12382–12387 (2006).
39. Chapman, M. J. & Mason, R. P. Cholesterol crystals and atherosclerotic plaque instability: therapeutic potential of eicosapentaenoic acid. *Pharmacol. Ther.* **240**, 108237 (2022).
40. Lange, Y. & Steck, T. L. Cholesterol homeostasis and the escape tendency (activity) of plasma membrane cholesterol. *Prog. Lipid Res.* **47**, 319–332 (2008).
41. Maxfield, F. R. & Tabas, I. Role of cholesterol and lipid organization in disease. *Nature* **438**, 612–621 (2005).
42. Zhu, J.-Y. et al. Mechanosensitive conjugated oligoelectrolytes for visualizing temporal changes in live cells. *Angew. Chem. Int. Ed.* **64**, e202506396 (2025).
43. Zhu, J.-Y. et al. Photophysics of conjugated oligoelectrolytes relevant to two-photon fluorescence-lifetime imaging microscopy. *Adv. Funct. Mater.* **33**, 2305962 (2023).
44. Zhu, J.-Y. & Bazan, G. C. Molecular orientation and optimization of membrane dyes based on conjugated oligoelectrolytes. *Cell Rep. Phys. Sci.* **4**, 101429 (2023).
45. Chan, S. J. W., Zhu, J.-Y., Yip, B. R. P., Shyamasundar, S. & Bazan, G. C. Molecular design of a diketopyrrolopyrrole conjugated oligoelectrolyte capable of imaging intracellular vesicle membrane dynamics. *Adv. Mater.* **37**, 2411329 (2025).
46. Wu, Y. et al. Molecular rheometry: direct determination of viscosity in Lo and Ld lipid phases via fluorescence lifetime imaging. *Phys. Chem. Chem. Phys.* **15**, 14986–14993 (2013).
47. Digman, M. A., Caiolfa, V. R., Zamai, M. & Gratton, E. The phasor approach to fluorescence lifetime imaging analysis. *Biophys. J.* **94**, L14–L16 (2008).

48. Kumarage, T. et al. Cholesterol modulates membrane elasticity via unified biophysical laws. *Nat. Commun.* **16**, 7024 (2025).
49. Zhang, Y., Li, Q., Dong, M. & Han, X. Effect of cholesterol on the fluidity of supported lipid bilayers. *Colloids Surf. B Biointerfaces* **196**, 111353 (2020).
50. Izri, Z., van der Linden, M. N., Michelin, S. & Dauchot, O. Self-propulsion of pure water droplets by spontaneous Marangoni-stress-driven motion. *Phys. Rev. Lett.* **113**, 248302 (2014).
51. Michelin, S., Lauga, E. & Bartolo, D. Spontaneous autophoretic motion of isotropic particles. *Phys. Fluids* **25**, 061701 (2013).
52. Scheidt, H. A., Huster, D. & Gawrisch, K. Diffusion of cholesterol and its precursors in lipid membranes studied by ^{1}H pulsed field gradient magic angle spinning NMR. *Biophys. J.* **89**, 2504–2512 (2005).
53. Edholm, O. & Nagle, J. F. Areas of molecules in membranes consisting of mixtures. *Biophys. J.* **89**, 1827–1832 (2005).
54. Shan, Y. & Wang, H. The structure and function of cell membranes examined by atomic force microscopy and single-molecule force spectroscopy. *Chem. Soc. Rev.* **44**, 3617–3638 (2015).
55. Touhami, A., Jericho, M. H. & Beveridge, T. J. Atomic force microscopy of cell growth and division in Staphylococcus aureus. *J. Bacteriol.* **186**, 3286–3295 (2004).
56. Nijenhuis, N., Zhao, X., Carisey, A., Ballestrem, C. & Derby, B. Combining AFM and acoustic probes to reveal changes in the elastic stiffness tensor of living cells. *Biophys. J.* **107**, 1502–1512 (2014).
57. Meister, A. et al. FluidFM: combining atomic force microscopy and nanofluidics in a universal liquid delivery system for single cell applications and beyond. *Nano Lett.* **9**, 2501–2507 (2009).
58. Grönbeck, H. & Zhdanov, V. P. Effect of lattice strain on hydrogen diffusion in Pd: a density functional theory study. *Phys. Rev. B* **84**, 052301 (2011).
59. Kim, J. et al. Quantitative evaluation of cardiomyocyte contractility in a 3D microenvironment. *J. Biomech.* **41**, 2396–2401 (2008).
60. Goffin, J. M. et al. Focal adhesion size controls tension-dependent recruitment of α-smooth muscle actin to stress fibers. *J. Cell Biol.* **172**, 259–268 (2006).
61. Galbraith, C. G. & Sheetz, M. P. Keratocytes pull with similar forces on their dorsal and ventral surfaces. *J. Cell Biol.* **147**, 1313–1324 (1999).
62. Rawicz, W., Olbrich, K. C., McIntosh, T., Needham, D. & Evans, E. Effect of chain length and unsaturation on elasticity of lipid bilayers. *Biophys. J.* **79**, 328–339 (2000).
63. Picas, L., Rico, F. & Scheuring, S. Direct measurement of the mechanical properties of lipid phases in supported bilayers. *Biophys. J.* **102**, L01–L03 (2012).
64. Sodt, A. J., Pastor, R. W. & Lyman, E. Hexagonal substructure and hydrogen bonding in liquid-ordered phases containing palmitoyl sphingomyelin. *Biophys. J.* **109**, 948–955 (2015).
65. Goodchild, J. A., Walsh, D. L. & Connell, S. D. Nanoscale substrate roughness hinders domain formation in supported lipid bilayers. *Langmuir* **35**, 15352–15363 (2019).
66. de Almeida, R. F., Fedorov, A. & Prieto, M. Sphingomyelin/phosphatidylcholine/cholesterol phase diagram: boundaries and composition of lipid rafts. *Biophys. J.* **85**, 2406–2416 (2003).
67. Biswas, A., Kashyap, P., Datta, S., Sengupta, T. & Sinha, B. Cholesterol depletion by MβCD enhances cell membrane tension and its variations-reducing integrity. *Biophys. J.* **116**, 1456–1468 (2019).
68. Das, A., Brown, M. S., Anderson, D. D., Goldstein, J. L. & Radhakrishnan, A. Three pools of plasma membrane cholesterol and their relation to cholesterol homeostasis. *eLife* **3**, e02882 (2014).
69. Sandhu, J. et al. Aster proteins facilitate nonvesicular plasma membrane to ER cholesterol transport in mammalian cells. *Cell* **175**, 514–529.e20 (2018).
70. Levental, I. et al. Cholesterol-dependent phase separation in cell-derived giant plasma-membrane vesicles. *Biochem. J.* **424**, 163–167 (2009).

Acknowledgements

Figures 1A, 4A, 5A and 6A and Supplementary Fig. 19A are original schematic illustrations prepared by the authors using BioRender.com, and the corresponding BioRender publication licence has been uploaded as a related manuscript file. No elements were reproduced from previously published figures or other external sources.

Author contributions

H.T. and N.-J.C. conceived the study and designed the research. H.T., Y.C., D.J., L.G. and S.P. performed the experiments. H.T. and Y.C. analyzed the data and interpreted the results. J.-Y.Z. and G.C.B. developed and characterized the COE-BY probe and contributed to the fluorescence lifetime imaging analysis and interpretation. V.P.Z. developed the mathematical framework and contributed to the theoretical analysis and interpretation. A.N.P. contributed to the interpretation of the results. N.-J.C. supervised the research. H.T. wrote the original manuscript. H.T., V.P.Z., A.N.P., and N.-J.C. revised the manuscript. All authors discussed the results, reviewed the manuscript, and approved the final version.

Funding

This work was supported by the Ministry of Education (MOE), Singapore, under Grant AcRF Tier 1 2020-T1-002-032 (RG111/20) awarded to N.-J.C., and by the CREATE Programme of the National Research Foundation, Singapore, awarded to N.-J.C. This work was also supported by the Ministry of Education (MOE), Singapore, under Grant MOE AcRF Tier 1 (RG34/22) awarded to N.-J.C., and by a sponsored research agreement from LUCA AICell Inc. (RCA-LUCA AICell REQ0239282) awarded to N.-J.C. The funders had no role in study design, data collection and analysis, decision to publish, or preparation of the manuscript. G.C.B. and A.N.P. acknowledge the support from the Singapore Ministry of Education (MOE) through its Research Center of Excellence award to the Institute for Digital Molecular Analytics & Science (IDMxS), NTU (EDUNC-33-18-279-V12-IDMxS).

Competing interests

N.-J.C. received research funding through a sponsored research agreement from LUCA AICell Inc. (RCA-LUCA AICell REQ0239282) that provided partial financial support for this work; the company had no role in the design of the study, in the collection, analysis or interpretation of the data, in the writing of the manuscript, or in the decision to submit it for publication. The remaining authors declare no competing interests.

Additional information

Supplementary information The online version contains supplementary material available at https://doi.org/10.1038/s41467-026-79445-1.

Correspondence and requests for materials should be addressed to Nam-Joon Cho.

Peer review information *Nature Communications* thanks the anonymous reviewer(s) for their contribution to the peer review of this work. A peer review file is available.

Reprints and permissions information is available at http://www.nature.com/reprints

Publisher's note Springer Nature remains neutral with regard to jurisdictional claims in published maps and institutional affiliations.

Open Access This article is licensed under a Creative Commons Attribution 4.0 International License, which permits use, sharing, adaptation, distribution and reproduction in any medium or format, as long as you give appropriate credit to the original author(s) and the source, provide a link to the Creative Commons licence, and indicate if changes were made. The images or other third party material in this article are included in the article's Creative Commons licence, unless indicated otherwise in a credit line to the material. If material is not included in the article's Creative Commons licence and your intended use is not permitted by statutory regulation or exceeds the permitted use, you will need to obtain permission directly from the copyright holder. To view a copy of this licence, visit http://creativecommons.org/licenses/by/4.0/.

© The Author(s) 2026